Advanced Functional Materials

ADVANCED FUNCTIONAL MATERIALS
www.afm-journal.de

RESEARCH ARTICLE

Strong-Binding Small-Molecule Passivator for Two-Dimensional Tin-Based Perovskite Field-Effect Transistors

Hyeonmin Choi[1] | Joonha Jung[1] | Young-Kwang Jung[2] | Seok Woo Lee[1] | Taehyun Kong[1] | Yongjin Kim[1] | Youjin Reo[3] | Jinwoo Sim[4] | Yeeun Kim[4] | Jaeyong Woo[4] | Sunggyu Ryoo[4] | Jaeyoon Cho[1] | Youcheng Zhang[5] | Stefano Pecorario[5] | Bo Ram Lee[6] | Henning Sirringhaus[5] | Yong-Young Noh[3] | Samuel D. Stranks[2] | Takhee Lee[4] | Keehoon Kang[1,7,8]

[1]Department of Materials Science and Engineering, and Research Institute of Advanced Materials, Seoul National University, Seoul, South Korea | [2]Department of Chemical Engineering and Biotechnology, University of Cambridge, Cambridge, UK | [3]Department of Chemical Engineering, Pohang University of Science and Technology, Pohang, Republic of Korea | [4]Department of Physics and Astronomy, and Institute of Applied Physics, Seoul National University, Seoul, South Korea | [5]Cavendish Laboratory, University of Cambridge, Cambridge, UK | [6]Department of Advanced Materials Science & Engineering, Sungkyunkwan University, Suwon, Republic of Korea | [7]Soft Foundry Institute, Seoul National University, Seoul, South Korea | [8]Institute of Applied Physics, Seoul National University, Seoul, South Korea

Correspondence: Takhee Lee (tlee@snu.ac.kr) | Keehoon Kang (keehoon.kang@snu.ac.kr)

Received: 3 December 2025 | **Revised:** 8 January 2026 | **Accepted:** 12 January 2026

ABSTRACT

2D layered tin halide perovskites are promising channel materials for field-effect transistors (FETs) owing to their high carrier mobility and lead-free composition, yet they suffer from severe defect sensitivity arising from facile Sn(II) oxidation. Here, we present a molecular design strategy that directly links passivator chemistry to device-level performance by synthesising a controlled pair of phosphine oxide Lewis bases—triphenylphosphine oxide (TPPO) and its methoxy-functionalised analogue (TMPPO)—to systematically tune Lewis basicity and coordination strength with undercoordinated Sn^{2+} sites. The stronger Lewis base TMPPO stabilises Sn^{2+}, yielding a twofold increase in hole mobility (up to 2.2 $cm^2\ V^{-1}\ s^{-1}$), negative threshold voltage shift, reduced hysteresis, and superior operational stability. These findings demonstrate that molecular basicity can be rationally translated into defect control and transistor performance, providing a general design principle for stable, high-performance, lead-free perovskite electronics.

1 | Introduction

Metal halide perovskites (MHPs) are crystalline semiconductors with the general formula ABX_3, where A is a monovalent cation (e.g., methylammonium$^+$, formamidinium$^+$, cesium$^+$), B is a divalent metal cation such as Pb^{2+} or Sn^{2+}, and X is a halide (Cl^-, Br^-, or I^-) [1, 2]. Their soft ionic lattice enables low-temperature processing, while their defect-tolerant electronic structure supports efficient charge transport despite structural imperfections [3]. These attributes have enabled MHPs to power a wide range of applications from solar cells [4–6] and LEDs [7–9] to electronic devices such as field-effect transistors (FETs) [10–12].

MHPs are promising FET channel materials due to their high carrier mobility (exceeding ~70 $cm^2\ V^{-1}\ s^{-1}$ for 3D Sn perovskite) [13], and compatibility with scalable device fabrication [14, 15].

Hyeonmin Choi, Joonha Jung, and Young-Kwang Jung contributed equally to this work

However, conventional 3D perovskites suffer from ion migration, environmental instability, and defect-induced hysteresis, all of which hinder their practical implementation in FETs [16, 17]. Among the various structural derivatives of metal halide perovskites, the Ruddlesden–Popper (RP) phase represents a 2D layered perovskite structure analogue formed by introducing bulky organic spacer cations such as phenylethylammonium (PEA), butylammonium (BA), and 4-fluorophenylethylammonium (4F-PEA) [18]. The resulting layered organic–inorganic architecture acts as a physical barrier to ion migration [19, 20] and improves environmental stability against moisture [21, 22].

Among MHPs, phenylethylammonium tin iodide $(PEA)_2SnI_4$ has emerged as a benchmark of 2D RP perovskite for FET studies since initial demonstration by Mitzi et al. [23, 24], owing to its lead-free composition and strong π–π stacking that promotes in-plane transport with reported field-effect mobilities for RP tin-halide perovskite FET channels typically spanning the ~0.1–10 $cm^2\ V^{-1}\ s^{-1}$ range [10, 25–31]. Nevertheless, these same structural features also make 2D RP perovskites less defect-tolerant than their 3D counterparts [32]. The alternating organic–inorganic layers enhance Coulomb interactions by reducing dielectric screening across the inorganic slabs, which increases defect localization and deepens trap levels [33, 34]. The challenge is particularly severe in tin-based systems, where Sn^{2+} readily oxidises to Sn^{4+} ($E° \approx -0.15$ V) [35], generating tin vacancies (V_{Sn}) that induce unintentional p-type doping, especially at surfaces and grain boundaries [16]. These intrinsic instabilities underscore the importance of defect passivation in tin-based RP phase perovskites [36, 37]. Among various chemical approaches, Lewis base molecules—bearing lone-pair electrons that can coordinate to undercoordinated metal centers—offer a rational means to stabilize Sn^{2+} and suppress the formation of deep defect states.

Building on this concept, additive engineering—using pseudo-halide anions [38], polymers [39], and Lewis base solvents (e.g., DMSO, urea) [40]—has provided improvements, but such strategies often alter crystallisation, making mechanistic attribution difficult. As a result, previous efforts have largely relied on empirical optimisation, leaving the link between chemical passivation and device-level outcomes unresolved [41, 42]. Therefore, a rational molecular design strategy is required that enables control over chemically defined parameters, such as binding affinity and Lewis basicity, thereby disentangling defect passivation effects from crystallisation influences.

In this study, we propose a molecular design strategy for defect passivation in RP tin-based perovskites by tuning the electron-donating ability of phosphine oxide passivators. Specifically, we validated the well-established **triphenylphosphine oxide (TPPO)** [43, 44] and developed its methoxy-functionalised analogue, **tris(4-methoxyphenyl)phosphine oxide (TMPPO)** as a reference and new defect passivator molecules employed for RP tin-based perovskites, $(PEA)_2SnI_4$, respectively. Through in-depth material and device characterisation, we establish how molecular basicity correlates with Sn^{2+} stabilisation and field-effect transistor performance. Specifically, TMPPO-treated devices exhibited a twofold increase in hole mobility (up to 2.2 $cm^2\ V^{-1}\ s^{-1}$) compared to pristine films, along with a reduced threshold voltage and suppressed hysteresis, confirming the enhanced defect passivation. This performance hierarchy, with TMPPO outperforming TPPO and the pristine counterpart, mirrors the increase in Lewis basicity, underscoring the effectiveness of rational molecular design in RP tin halide perovskites.

2 | Results and Discussion

We utilised $(PEA)_2SnI_4$, a tin-based RP perovskite chosen for its ability to form highly ordered layered structures favorable for charge transport [45, 46]. Atomic force microscopy (AFM) revealed well-defined 2D terraces with an interlayer spacing of 1.6–1.7 nm (Figure S1), confirming the formation of a crystalline layered film. Grain-edge features were more pronounced in AFM than in scanning electron microscopy (SEM) images (Figures S2 and S3), likely due to electron-beam-induced surface damage. Dark-field (DF) microscopy further confirmed instability under ambient conditions, showing time-dependent degradation at grain boundaries, evident from increased light scattering (Figure S4), which is consistent with progressive surface oxidation.

To overcome defect formation and spontaneous oxidation of Sn^{2+} in RP tin halide perovskites (Figure 1a), phosphine oxide-based Lewis base molecules were incorporated into the perovskite precursors to passivate undercoordinated Sn sites. TPPO was selected as the primary passivator for its strong affinity to B-site metal cations, effectively reducing surface defects and stabilising the lattice [45, 46]. Building on this, we introduced a methoxy-functionalised analogue, TMPPO, to enhance Lewis basicity and strengthen Sn^{2+} coordination. (Figure S5). The introduction of methoxy groups increases the electron density around the phosphine oxide moiety, enhancing the Lewis basicity of TMPPO compared to TPPO. Figure 1b shows electrostatic surface potential (ESP) maps from density functional theory (DFT), highlighting distinct charge distributions that define Lewis base strength. The P═O group exhibited ESP values of −48.31 kcal/mol for TPPO and −53.23 kcal/mol for TMPPO, confirming the higher basicity of TMPPO.

The perovskite precursor solution was prepared using a DMSO-based co-solvent processing strategy for TPPO and TMPPO molecular additives incorporated as passivators. DMSO, though having a weaker binding energy with SnI_2 (−0.639 eV) than TPPO (−0.804 eV) or TMPPO (−0.873 eV), plays a dominant role in crystallisation by forming intermediate phases with SnI_2 and slowing grain growth (Figure 1c) [47]. During annealing, DMSO evaporates, whereas the non-volatile TPPO and TMPPO remain in the film and passivate undercoordinated Sn^{2+} sites and halide-related defects. This co-solvent approach promotes uniform and stable grain growth while avoiding the film degradation often seen in post-deposition treatments, as evidenced by the consistent morphology observed across all samples (Figure S2) [48].

We first investigated how the Lewis basicity of the two passivators affects the structural and electrical properties of $(PEA)_2SnI_4$ perovskite films. To verify that the incorporation of passivator molecules does not affect the structural integrity of the $(PEA)_2SnI_4$ lattice, thin-film X-ray diffraction (XRD) was performed, and the resulting patterns for pristine, TPPO-treated, and TMPPO-treated films all exhibited distinct (002), (004), (006), and (008) reflections corresponding to the periodic stacking of the 2D layered perovskite structure (Figure 2a). The identical peak

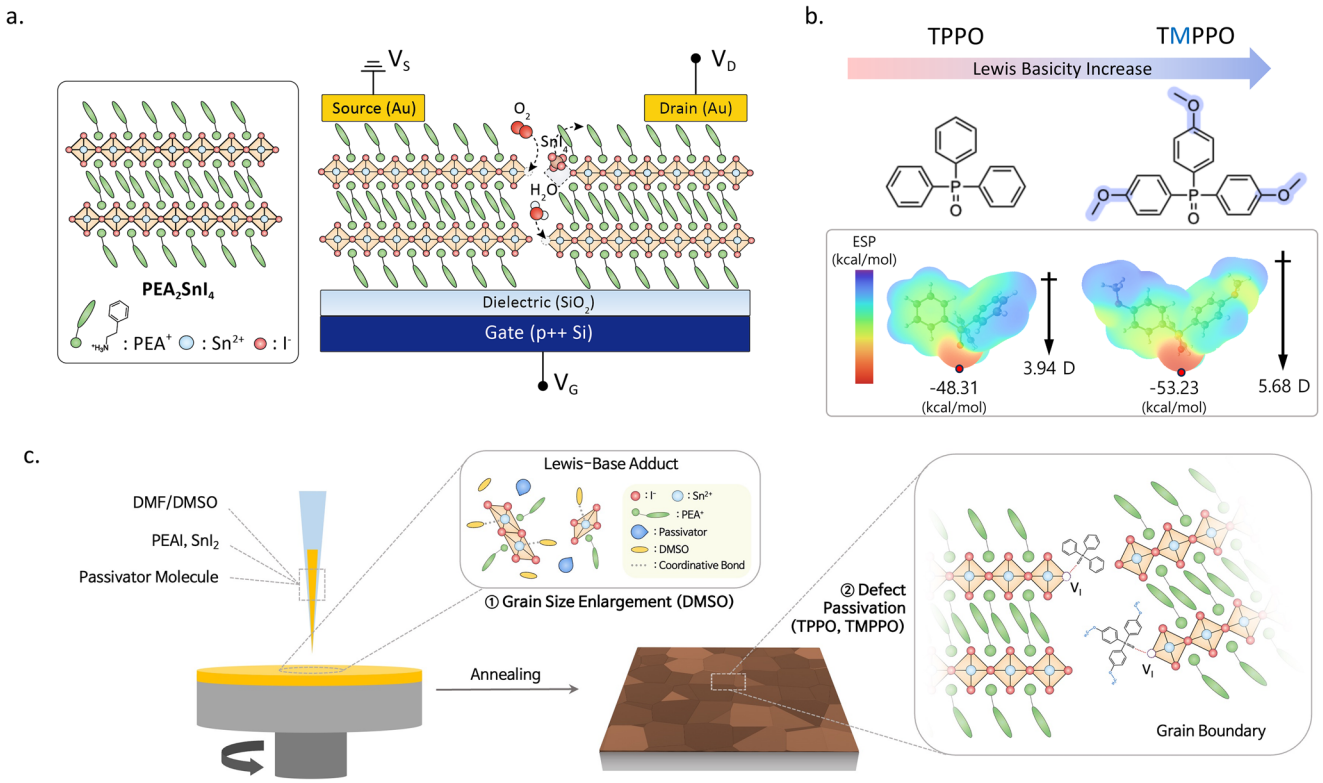

FIGURE 1 | (a) Schematic illustration highlighting the necessity of defect passivation in 2D tin halide perovskites, (b) Molecular structures and electrostatic potential (ESP) maps and dipole moments of TPPO and TMPPO, calculated by density functional theory (DFT). The ESP values at the P = O sites are −48.31 kcal/mol for TPPO and −53.23 kcal/mol for TMPPO. The corresponding dipole moments are 3.94 D and 5.64 D, respectively. (c) Schematic illustration of the crystallisation and defect passivation processes in the $(PEA)_2SnI_4$ thin film.

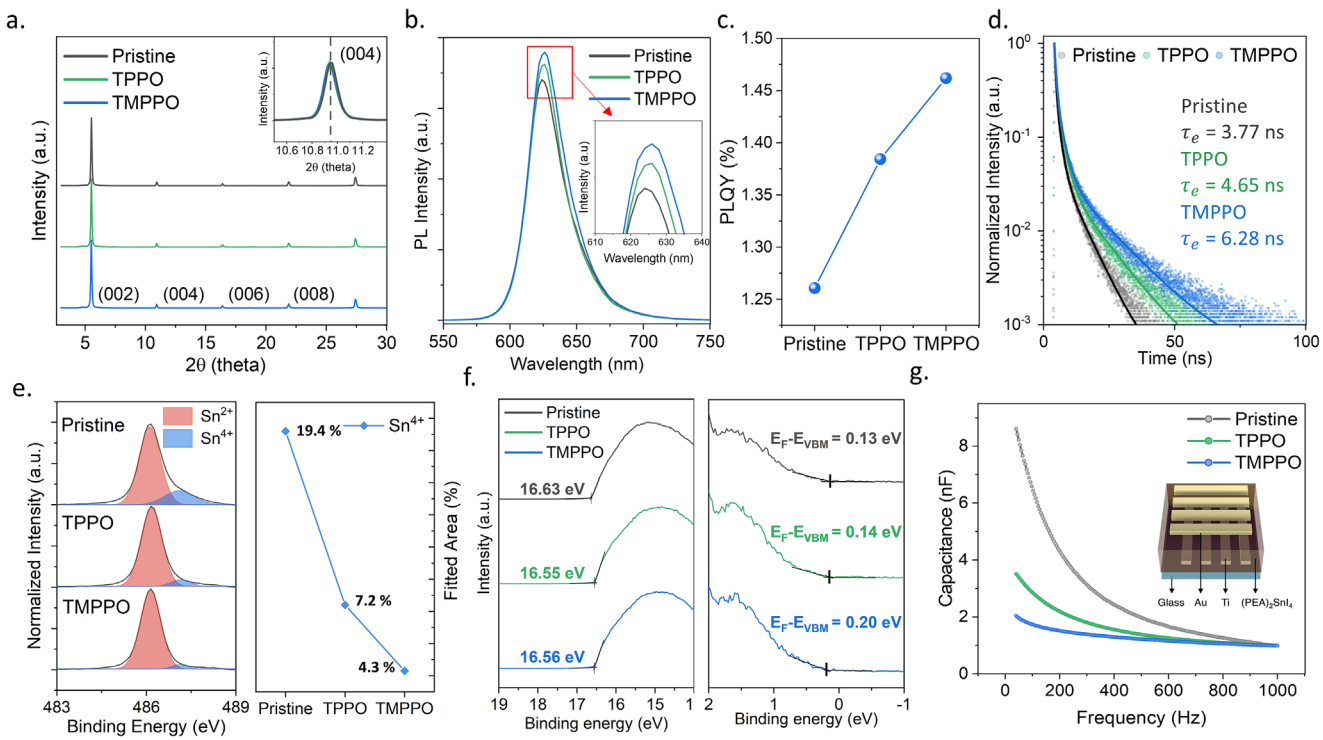

FIGURE 2 | Characterization of pristine, TPPO-treated, and TMPPO-treated $(PEA)_2SnI_4$ perovskite thin films: (a) X-ray diffraction (XRD) patterns, (b) photoluminescence (PL) spectra, (c) photoluminescence quantum yield (PLQY), (d) time-resolved photoluminescence (TRPL) decays, (e) X-ray photoelectron spectroscopy (XPS) spectra, (f) ultraviolet photoelectron spectroscopy (UPS) spectra, and (g) capacitance-frequency (C–f) characteristics measured using a cross-bar array structure.

positions ($2\theta \approx 5.5°$) and narrow full width at half maximum (FWHM ≈ 0.12°) observed across all samples indicate that the lattice remains undistorted. Moreover, the interlayer spacing d_{200} , calculated to be 1.6 nm, aligns closely with AFM line profile results shown in Figure S1.

Photoluminescence (PL) and photoluminescence quantum yield (PLQY) measurements were performed to assess the optical properties of passivator-treated $(PEA)_2SnI_4$ films (Figure 2b,c). The main PL peak of the pristine film at ~630 nm, consistent with its optical bandgap, remained unchanged after passivation (Figure S6). However, both PL intensity and PLQY increased with passivator basicity — highest for TMPPO, followed by TPPO and pristine — confirming the correlation between Lewis basicity and radiative efficiency [49, 50]. Specifically, PLQY values increased from 1.26 % (pristine) to 1.38 % (TPPO) and 1.46 % (TMPPO). This enhancement is further supported by PLQY degradation traces measured under ambient conditions (Figure S7). The TRPL decay curves were fitted using a tri-exponential model (see Section S3). The extracted average lifetime showed a similar trend, with average exciton lifetimes of 6.3 ns (TMPPO), 4.6 ns (TPPO), and 3.8 ns (pristine). The extended lifetime with stronger passivators further confirms effective trap reduction [51]. Importantly, the consistent grain size (~15 μm) across all samples indicates that these improvements arise from defect passivation rather than morphological changes.

To verify whether the defect suppression is accompanied by reduced Sn degradation, we performed X-ray photoelectron spectroscopy (XPS) on $(PEA)_2SnI_4$ films. Samples were analysed after 0 and 30 min of air exposure, then transferred to a vacuum chamber to prevent further degradation. At 0 min, pristine, TPPO-, and TMPPO-treated films showed identical spectra (Figure S8). After 30 min, pristine films displayed clear Sn^{4+} shoulder peaks at 487 eV (Figure 2e), corresponding to 19.4 % Sn^{4+}, whereas TPPO- and TMPPO-treated films showed only 7.2 % and 4.3 %, respectively. This confirms that passivators strongly mitigate Sn^{2+} oxidation, with TMPPO most effective, consistent with its higher Lewis basicity. Notably, this reduction in Sn^{4+} content reflects suppression of Sn^{4+} formation rather than a chemical reduction of pre-existing Sn^{4+} species.

While XPS confirms the chemical changes in the oxidation states, it is also crucial to understand how these changes affect the electronic structure of the material. To explore the influence of Sn oxidation on the band structure, we performed ultraviolet photoelectron spectroscopy (UPS) (Figure 2f). The UPS analysis revealed that the energy separation between the Fermi level (E_F) and the valence band maximum (VBM) increased from 0.13 eV in the pristine film to 0.14 and 0.20 eV for the TPPO- and TMPPO-treated samples, respectively, indicating a shift of E_F away from the VBM due to reduced p-type self-doping induced by Sn(IV) defects. (Figure S9). This behavior is in line with Sn(II) oxidation that promotes the formation of tin vacancies (V_{Sn}), which act as acceptor-like defects [35, 52–54]. However, the addition of strong Lewis base molecules, such as TMPPO, effectively reduces the formation of Sn^{4+}, thereby weakening the degree of *p*-type doping.

Since Sn(II) oxidation and ion migration jointly limit stability, we measured the ionic response by capacitance–frequency (C–f) (Figure 2g). At low frequencies (<100 Hz), the pristine films showed the highest capacitance due to charge accumulation from mobile defects, whereas the TMPPO-treated films exhibited the lowest, indicating suppressed ion migration through effective defect passivation [55]. At high frequencies, all samples converged, consistent with freeze-out of ionic motion. Contact-angle measurements (Figure S10) further confirmed enhanced hydrophobicity in passivated films, supporting improved ambient stability.

To probe the microscopic origin of passivation, we investigated passivator–Sn interactions by ^{31}P NMR. In solution, TPPO and TMPPO exhibited chemical shifts at 29.45 and 30.14 ppm (Figure 3a). Upon coordination with SnI_2, both shifted downfield, with TMPPO showing a larger shift ($\Delta\delta$ = 2.28 vs. 0.60 ppm), indicating relatively stronger P═O─Sn^{2+} bonding. Solid-state ^{31}P NMR of SnI_2 mixed with passivators (Figure 3b) confirmed this trend: while most molecules remained unbound, a fraction shifted downfield, with TMPPO showing a higher bonded proportion (58 %) than TPPO (41 %). These results corroborate that TMPPO forms stronger and more abundant coordination bonds with Sn^{2+}.

To gain the underlying atomistic insights of defect passivation, we performed density functional theory (DFT) calculations by considering surface adsorption of the defect passivators at the edges of the $(PEA)_2SnI_4$ perovskite lattice. First, we assessed the strength of the chemical bonding between P═O moieties of the passivators and undercoordinated Sn^{2+} sites at the edge of $(PEA)_2SnI_4$. The local atomic geometries of the $(PEA)_2SnI_4$ edge with TPPO and TMPPO are shown in Figure 3c (full atomic models are provided in Figure S11). The adsorption energy (E_{ads}) of TPPO and TMPPO molecules on the edge of $(PEA)_2SnI_4$ was calculated as: $E_{ads} = E_{(PEA)_2SnI_4+\ passivator} - (E_{(PEA)_2SnI_4} + E_{passivator})$where $E_{(PEA)_2SnI_4+\ passivator}$, pristine $E_{(PEA)_2SnI_4}$, and $E_{passivator}$ represent the DFT total energies of the passivated $(PEA)_2SnI_4$ edge, pristine $(PEA)_2SnI_4$ edge, and the isolated passivator molecule in the gas phase, respectively.

The calculated E_{ads} is −1.20 eV for TPPO and −1.38 eV for TMPPO, indicating TMPPO binds more strongly to Sn^{2+} at the edge than TPPO. The spatial distribution of charge accumulation and depletion regions (Figure 3c) shows that both passivators form similar chemical bonds, but the planar-integrated charge density difference (CDD) plot (Figure 3d) confirms that TMPPO exhibits slightly larger fluctuation in the CDD profile near the binding site compared to TPPO. This is attributed to the enhanced Lewis basicity of TMPPO, which results in stronger binding. Notably, the stronger binding of TMPPO can also be predicted in 3D tin perovskite systems, as evidenced by DFT calculations on $CsSnI_3$, which reflects the generality of our Lewis-basicity-based defect passivation concept (Figure S12).

We further analysed the density of states of the $(PEA)_2SnI_4$ edge before and after passivation to understand the role of the passivators. It is well-known that Sn *s*-orbital predominantly contributes to valence band maximum (VBM) states in tin-based RP perovskites [27]. Partial density of states plots of the Sn *s*-orbital for Sn atoms in the bulk region and at the edge are shown in Figure 3e. In the pristine edge (before passivation), the

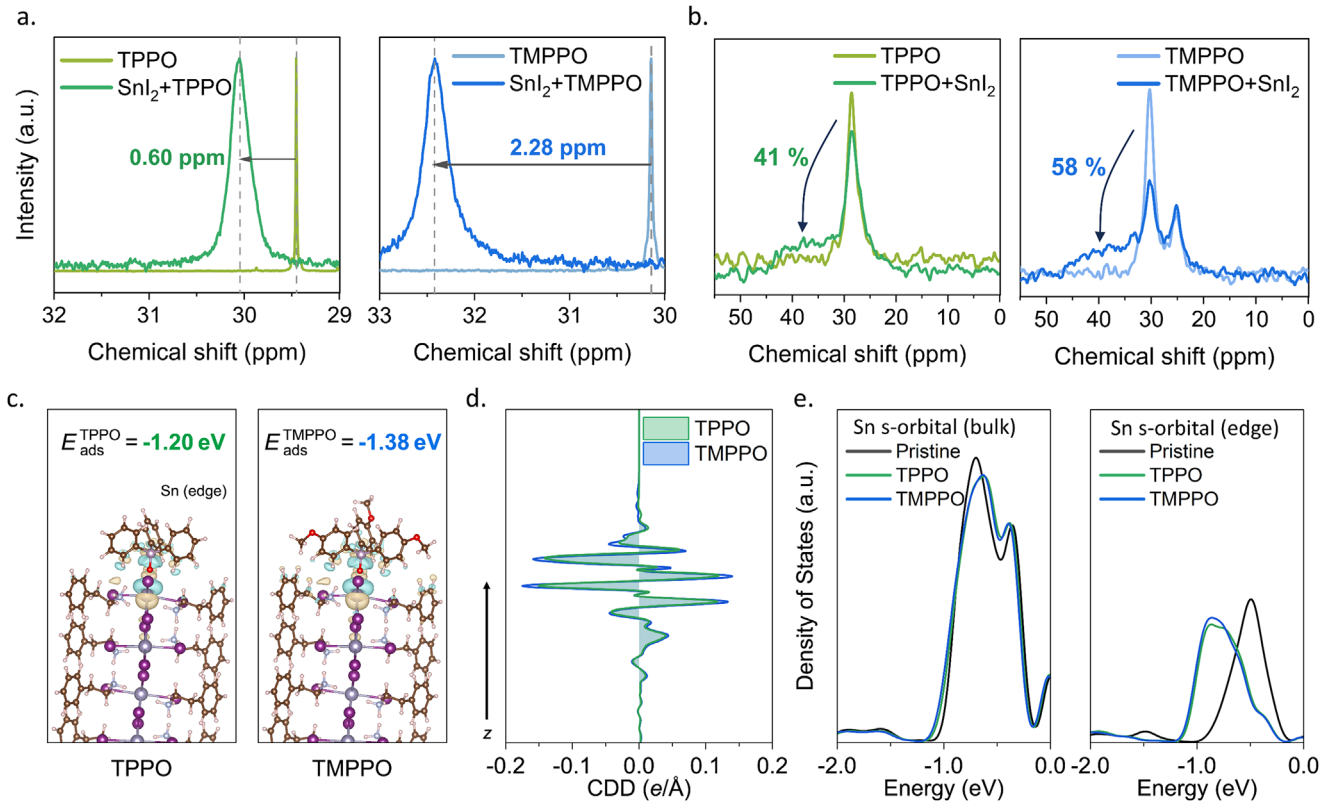

FIGURE 3 | (a) ^{31}P Solution NMR and (b) ^{31}P Solid-State NMR of pure passivator molecules and TPPO & TMPPO incorporated with SnI_2. (c) Local atomic structures of the $(PEA)_2SnI_4$ edge with TPPO and TMPPO adsorbed onto undercoordinated Sn^{2+} sites at the edge. The electron accumulation and depletion regions are indicated in yellow and blue, respectively. (d) Planar-integrated charge density difference (CDD) plots corresponding to (c). (e) Partial density of states (DOS) of Sn s-orbital for the pristine edge, TPPO-passivated edge, and TMPPO-passivated edge of $(PEA)_2SnI_4$. Sn atoms in the bulk region and at the edge are compared (see Figure S11 for the definition of bulk and edge). Energy is referenced to the bulk VBM, which is set to 0 eV.

first peak of Sn *s*-orbital states for edge Sn atoms is located at approximately −0.5 eV relative to the bulk VBM. Upon adsorption of the passivators on edge Sn sites, the Sn *s*-orbital states shift to lower energy levels with the first peak appearing near −1 eV. This suggests that the chemical bonding formed by the passivators stabilises Sn *s*-states of the undercoordinated Sn at the edge and makes it more difficult to extract electrons from these sites. As a result, oxidation from Sn(II) to Sn(IV) is effectively suppressed.

The key findings of the significant effect of defect passivation by the strongly binding Lewis base molecules, as demonstrated in previous sections, can be consolidated by their impact on the FET device performance. FET devices were fabricated using a conventional back-gate, top-contact (BGTC) structure on a 200 nm SiO_2/*p*++-Si substrate to investigate the charge transport properties of the $(PEA)_2SnI_4$ films, as described in the Methods section and illustrated in Figures S13 and S14. Figure 4a presents the transfer curves of the studied FETs made with pristine, TPPO-treated, and TMPPO-treated films, while the corresponding cycle-speed-dependent transfer curves and output curves are shown in Figures S15 and S16; the corresponding statistical distributions of key device parameters are summarized in Figure 4b and Figure S17. All devices exhibited typical p-type transport characteristics with an anti-clockwise hysteresis curve and an On/Off current ratio of 10^5, consistent with previous reports [27]. TMPPO-treated devices displayed nearly double the mobility of pristine films (1.9 vs. 1.0 $cm^2\ V^{-1}\ s^{-1}$) with the highest value reaching 2.2 $cm^2\ V^{-1}\ s^{-1}$, accompanied by a pronounced negative threshold shift (7.3 V vs. −6.5 V), thereby accessing a low-voltage regime that is typically inaccessible in 3D Sn perovskites due to their intrinsically high hole densities. The performance hierarchy, summarised in Table S1, highlights that TMPPO-passivated $(PEA)_2SnI_4$ achieves concurrent enhancements in mobility and stability compared to previously reported RP perovskite FETs.

To evaluate the validity of the strategy, we further tested devices processed with different solvent systems (DMF-only and DMF/DMSO). Across both conditions, the incorporation of TPPO and TMPPO consistently yielded step-like mobility improvements (0.56 $cm^2/V{\cdot}s$ for pristine, 0.71 $cm^2/V{\cdot}s$ for TPPO-treated, and 0.80 $cm^2/V{\cdot}s$ for TMPPO-treated films in the DMF-only system). The mixed DMF/DMSO system produced the highest device performance due to its crystallisation retardation effect, which promoted larger perovskite grains and facilitated more effective passivation [56]. Detailed data for the DMF-only system are provided in Figures S18–S21.

Analysis of the transfer curves revealed that passivation consistently drove V_{th} negative (7.3 V → 3.1 V → −6.5 V for pristine, TPPO, and TMPPO, respectively). In parallel, the hysteresis window decreased from 13.2 V (pristine) to 9.6 V (TPPO) and 5.2 V (TMPPO), confirming that stronger Lewis basicity progressively

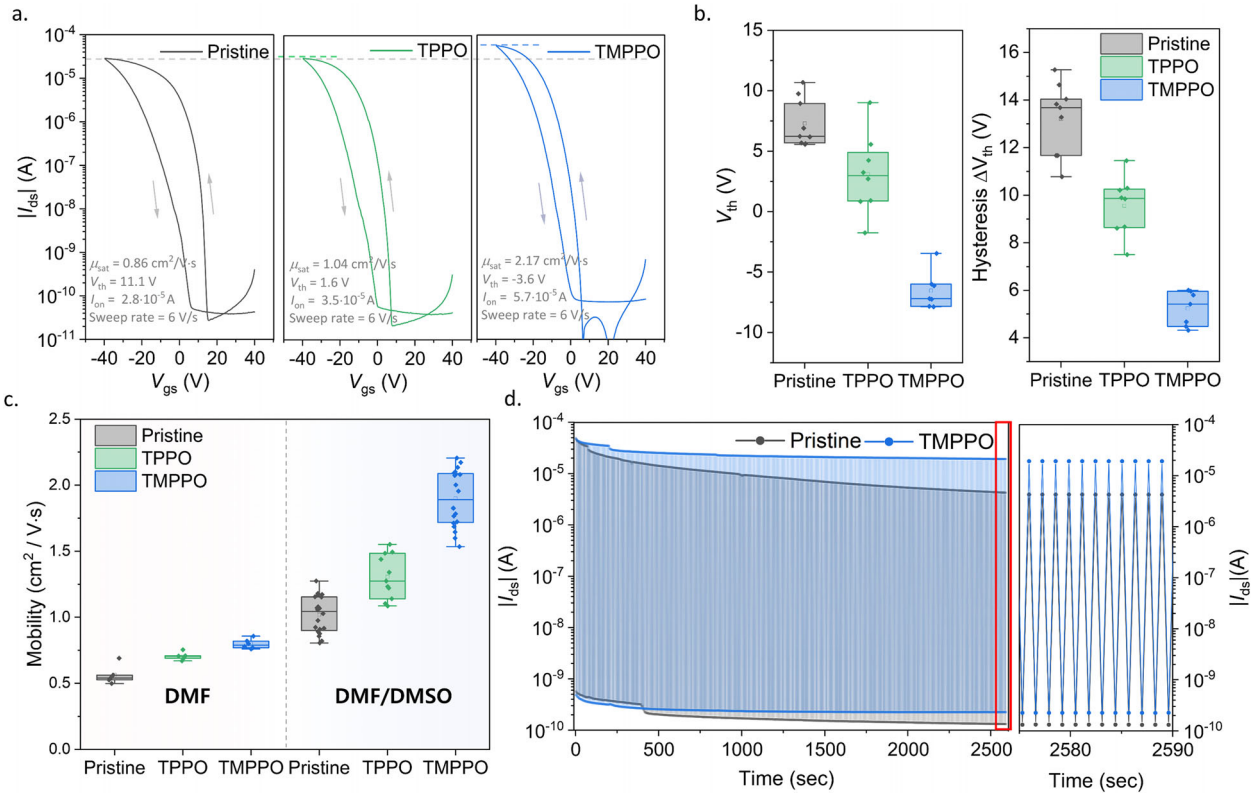

FIGURE 4 | (a) Transfer characteristics (I_{ds}-V_{gs}) of pristine, TPPO-treated, and TMPPO-treated $(PEA)_2SnI_4$ FETs measured at V_{ds} = −40 V, highlighting differences in on/off ratio, threshold voltage and mobility at sweep rate 6 V/sec, (b) Extracted threshold voltage (V_{th}) and hysteresis window showing systematic improvement with passivation (V_{th} = 7.3, 2.1, −6.5 V; hysteresis = 13.2, 9.6, 5.2 V), (c) Hole mobility values of pristine, TPPO-treated, and TMPPO-treated devices extracted from the saturation regime, demonstrating enhanced transport performance upon passivation, (d) Operational stability test (2000 cycle) under continuous bias stress (V_{ds} = −40 V), comparing the degradation behavior of the pristine device vs. the TMPPO-treated device over time.

suppresses self-doping effects of Sn. To evaluate the contribution of interface traps, we analyzed the subthreshold swing (SS) characteristics (Figure S15). The modest change in SS (1.26 → 1.18 → 1.19 V dec^{-1}) suggests that the pronounced negative V_{th} shift is dominated by reduced bulk self-doping rather than interface trap passivation. This degree of threshold tunability and hysteresis suppression marks a key distinction from both 3D Sn FETs and previous additive-engineered RP systems, where unintentional doping and trap states usually prevent low-threshold operation [30, 31, 57]. These trends align with suppressed Sn(II) oxidation (XPS) and stabilisation of the valence-band energetics (UPS), confirming the mechanistic role of Lewis basicity in governing defect physics.

The stability of the devices was further evaluated through both dynamic on/off switching and constant bias stress tests. As shown in Figure 4d, the TMPPO-passivated device exhibited improved operational stability, retaining ~50 % of its on-state current after 2000 switching cycles, whereas the pristine device degraded by nearly one order of magnitude under identical conditions. Under constant source-drain bias (V_{ds} = −1 V), pristine devices showed a rapid exponential decay of on-state current with a pronounced negative shift in threshold voltage (V_{th}) (Figures S22 and S23), consistent with degradation driven by positively charged iodide vacancy (V_I) migration [58]. In contrast, TMPPO-treated devices displayed only gradual current decay and inferior V_{th} variation.

3 | Conclusions

In conclusion, we demonstrate that the Lewis basicity of molecular passivators provides a rational and tunable pathway for defect control in RP tin halide perovskite FETs. By systematically comparing triphenylphosphine oxide (TPPO) and its methoxy-functionalised analogue (TMPPO), we reveal that stronger Lewis bases more effectively coordinate undercoordinated Sn^{2+}, suppress Sn(II) oxidation, and mitigate trap-assisted ion migration. This strengthened Sn^{2+}–Lewis base coordination intrinsically stabilises the perovskite lattice and suppresses vacancy formation, resulting in nearly two fold higher mobility, a large negative threshold shift, reduced hysteresis, and remarkable operational stability. These findings establish molecular basicity as a general design principle for effective defect passivation by strong binding and provide a concrete chemical route toward stable, high-performance, lead-free perovskite electronics.

4 | Experimental Section

4.1 | Organic Synthesis of Passivator Molecules

Triphenylphosphine oxide (TPPO) was obtained by directly oxidising Triphenyl phosphine (TPP), which was purchased from Sigma–Aldrich, with hydrogen peroxide (H_2O_2). TPP 1 g

(= 3.81 mmol) was stirred vigorously in Dichloromethane (DCM) with a solution of H_2O_2 (30 wt. %), 10 mL in D.I water for 2.5 h. After 3 times of work-up, the extracted solution was dried with magnesium sulphate ($MgSO_4$). DCM was then evaporated under low pressure (~480hPa) with 80 rpm rotation and temperature set at 35°C to the crude product. For column chromatography (CC), 100 mL of silica gel was packed with hexane with sea salt as the protecting layer and THF as the eluent. The dissolved solvent (THF + TPPO + impurities) was purified by CC, and THF was evaporated at low pressure (~480 hPa) at 60°C. Finally, TPPO was crystallised with hexane, and white powder (= TPPO) was collected by filtering the purified solution with a 0.45 μm membrane filter. Tris (4-methoxyphenyl) phosphine (TMPP) was obtained by adding 2.5 M hexane solution (11.43 mL) of n-BuLi solution dropwise to an agitating super-dry THF solution (60 mL) of 4-bromoanisole 5 g (= 26.73 mmol) at −78°C under an inert atmosphere of nitrogen. After stirring for 1 h, PCl_3 (0.6 mL) was added slowly, and the reaction mixture was stirred for 12 h. D.I water was added to quench the remaining n-BuLi. After 3 times work-up with MC, the organic phase was dried over $MgSO_4$ and filtered. The solvents (THF and hexane) were then evaporated under low pressure (~480 hPa) with 80 rpm rotation and temperature set at 50°C. The crude product was further purified by CC using hexane:THF = 7:1 as the eluent. Lastly, the solvent (hexane + THF) was evaporated under low pressure (~480 hPa) at 60°C and TMPP was crystallised at low temperature (−18°C). Tris (4-methoxyphenyl) phosphine oxide (TMPPO) was obtained with the same procedure as TPP oxidation to TPPO. Finally, the two organic molecules or passivators (TPPO, TMPPO) were confirmed with ^{1}H-NMR spectroscopy (solvent = $CDCl_3$) and FT-IR (solvent = DMF).

4.2 | $(PEA)_2SnI_4$ Thin Film Fabrication

Phenethylammonium iodide (PEAI) (purchased from Greatcell Solar Materials), tin(II) iodide (SnI_2) (99.99 % trace metals basis), dimethyl sulfoxide (DMSO, anhydrous, ≥99.9 %), and dimethylformamide (DMF, anhydrous, 99.8 %) were purchased from Sigma–Aldrich. The perovskite precursor solution was prepared by dissolving PEAI and SnI_2 in a DMF:DMSO mixed solvent (4:1 by volume) with a total precursor concentration of 0.1 M and a molar ratio of PEAI:SnI_2 = 2.3:1. Passivator molecules (TPPO or TMPPO) were added at 1 mol % relative to SnI_2, and the solution was stirred for 2 h at 60°C in a nitrogen-filled glovebox. After cooling the precursor for 30 min, the precursor was spin-coated (4000 rpm, 30 s) on glass substrates and Si/SiO_2 substrates, which were sonicated in acetone, isopropyl alcohol (IPA), and D.I. water consecutively for 10 min each, followed by UV-ozone treatment for 30 min. After annealing the thin films for 10 min at 100°C, we obtained Pristine, TPPO-treated, and TMPPO-treated thin films and conducted various thin film analysis experiments.

4.3 | $(PEA)_2SnI_4$ Thin Film Analysis

The XRD spectra were obtained with D8 Advance, 2020(multi-purpose XRD). The PL and PLQY of the $(PEA)_2SnI_4$ thin films were characterised using a spectrofluorometer (FP-8550ST, JASCO) with a 300 W Xenon arc lamp (excitation wavelength = 420 nm), and the absorption spectrum was obtained with a UV–vis spectroscopy (V-770, JASCO). The TRPL spectra were obtained through a confocal fluorescence lifetime image microscope system (FluoTime 300, PicoQuant). SEM images were obtained with an accelerating voltage of 15 kV (SU-70, Hitachi). XPS and UPS were conducted by ESCA Axis Supra+ installed at the National Center for Inter-university Research Facilities(NCIRF) at Seoul National University. The AFM image and line profile were obtained by (Park NX-10). For the capacitance–frequency (C–f) measurements, the perovskite layer was sandwiched between Ti/Au bottom and Au top electrodes. The measurements were carried out over a frequency range from 40 Hz to 1 kHz using a Keysight 4294A precision impedance analyzer with an AC signal amplitude of 100 mV. The effective device area was 1 mm^2. The water contact angle was calculated using the ImageJ program.

4.4 | Density Functional Theory (DFT) Calculations

Underlying density functional theory (DFT) calculations we performed based on Kohn–Sham DFT [59] as implemented in Vienna Ab Initio Simulation Package (VASP) [60, 61]. The projector augmented-wave (PAW) [62, 63] pseudopotentials are used to treat core atomic states, and the valence states of H, C, N, O, P, Sn, and I were treated explicitly by $1(1s^1)$, $4(2s^22p^2)$, $5(2s^22p^3)$, $6(2s^22p^4)$, $5(3s^23p^3)$, $14(4d^{10}5s^25p^2)$, $7(5s^25p^5)$ electrons, respectively. For the exchange-correlation functional, we employed the Perdew–Burke–Ernzerhof (PBE) [64] functional combined with the Grimme D3 dispersion correction (PBE + D3) [65]. To model the edge of $(PEA)_2SnI_4$, a symmetric (100) surface slab model with 658 atoms consisting of 7 octahedral layers and a vacuum region of 30 Å, was used. The atomic positions were fully relaxed while keeping the innermost octahedral layer fixed to the bulk values. A plane-wave energy cutoff of 700 eV and a Γ-centered 4 × 1 × 1 k-point mesh were used in all computations. The convergence thresholds were set to 10^{-6} eV for total energy and 10^{-2} eV/Å for atomic forces.

4.5 | ^{31}P-NMR

For solution ^{31}P-NMR (300 MHz, Bruker), we mixed 10 mg (0.027 mol) of SnI_2 with the same molar ratio of each passivator (0.027 mol of TPPO, TMPPO) in 1 mL of $CDCl_3$ and stirred the solution for 1.5 h in a glove box filled with N_2. For the solid-state ^{31}P-NMR, we hand-grinded SnI_2 and the passivator (with the same molar ratio) rigorously for 10 min per sample in a glove box filled with N_2. We obtained the ss-NMR (500 MHz, Bruker) spectra using a disposable insert, and the ^{31}P-signals were analysed with SpinWorks 4.

4.6 | $(PEA)_2SnI_4$ FET Fabrication and Characterization

A 200 nm thick SiO_2/p++-Si substrate was sequentially cleaned using acetone, isopropyl alcohol, and deionised (DI) water for 10 min each, followed by drying in a nitrogen gas flow. The substrates were then treated with UV-ozone for 30 min to remove organic residues and improve surface wettability. Immediately

after the UV-ozone treatment, the samples were quickly transferred into a glovebox to do the spin coating method. The prepared perovskite solution was spin-coated onto the substrates at 4000 rpm for 30 s to form $(PEA)_2SnI_4$ films, which were subsequently annealed at 100°C for 10 min. Au contacts were deposited onto the perovskite films using a shadow mask to fabricate top-contact devices. The channel length (L) and width (W) were approximately 200 and 1000 μm, respectively. For device characterisation, all FET measurements were conducted using a Keithley 4156B semiconductor parameter analyser under dark conditions at room temperature. The measurements were performed in a vacuum probe station, where the pressure was maintained at approximately 10^{-3} Torr to ensure accurate device performance assessment.

Acknowledgements

The authors appreciate the financial support of the National Research Foundation of Korea (NRF) grant (Nos. RS-2024-00342191, RS-2024-00404442, RS-2025-02305568, 2021M3H4A1A02049651, RS-2021-NR059728), the Samsung Research Funding & Incubation Center of Samsung Electronics under project number SRFC-MA2401-03. This work was supported by K-CHIPS (Korea Collaborative & High-tech Initiative for Prospective Semiconductor Research) (RS-2025-02305568, 25064-15TC) funded by the Ministry of Trade, Industry & Energy (MOTIE, Korea). Via our membership of the UK's HEC Materials Chemistry Consortium, which is funded by EPSRC (EP/X035859/1), this work used the ARCHER2 UK National Supercomputing Service (http://www.archer2.ac.uk). Y.-K.J. acknowledges UKRI guarantee funding for Marie Skłodowska-Curie Postdoctoral Fellowship 2021 (EP/X025756/1) and the Leverhulme Trust funding (RPG-2021-191). S.D.S. acknowledges the Royal Society and Tata Group (Grant Number UF150033, URF/R/221026). We also thank J. Lee for helpful discussions regarding the NMR analysis.

Conflicts of Interest

The authors declare no conflict of interest.

Data Availability Statement

The data that support the findings of this study are available from the corresponding author upon reasonable request.

References

1. T. M. Brenner, D. A. Egger, L. Kronik, G. Hodes, and D. Cahen, "Hybrid Organic—Inorganic Perovskites: Low-Cost Semiconductors With Intriguing Charge-Transport Properties," *Nature Reviews Materials* 1 (2016): 15007, https://doi.org/10.1038/natrevmats.2015.7.

2. J. Euvrard, Y. Yan, and D. B. Mitzi, "Electrical Doping in Halide Perovskites," *Nature Reviews Materials* 6 (2021): 531–549, https://doi.org/10.1038/s41578-021-00286-z.

3. J. Huang, Y. Yuan, Y. Shao, and Y. Yan, "Understanding the Physical Properties of Hybrid Perovskites for Photovoltaic Applications," *Nature Reviews Materials* 2 (2017): 17042, https://doi.org/10.1038/natrevmats.2017.42.

4. R. Lin, J. Xu, M. Wei, et al., "All-perovskite Tandem Solar Cells With Improved Grain Surface Passivation," *Nature* 603 (2022): 73–78, https://doi.org/10.1038/s41586-021-04372-8.

5. A. Cho and N. Park, "Impact of Interfacial Layers in Perovskite Solar Cells," *Chemsuschem* 10 (3687): 3687–3704, https://doi.org/10.1002/cssc.201701095.

6. Z. Shi, J. Guo, Y. Chen, et al., "Lead-Free Organic–Inorganic Hybrid Perovskites for Photovoltaic Applications: Recent Advances and Perspectives," *Advanced Materials* 29 (2017): 1605005, https://doi.org/10.1002/adma.201605005.

7. J. S. Kim, J.-M. Heo, G.-S. Park, et al., "Ultra-bright, Efficient and Stable Perovskite Light-emitting Diodes," *Nature* (2022): 1–7, https://doi.org/10.1038/s41586-022-05304-w.

8. C. Sun, Y. Jiang, M. Cui, et al., "High-Performance Large-Area Quasi-2D Perovskite Light-emitting Diodes," *Nature Communications* 12 (2021): 2207, https://doi.org/10.1038/s41467-021-22529-x.

9. Y. Hassan, J. H. Park, M. L. Crawford, et al., "Ligand-engineered Bandgap Stability in Mixed-halide Perovskite LEDs," *Nature* 591 (2021): 72–77, https://doi.org/10.1038/s41586-021-03217-8.

10. Y. Liang, F. Li, and R. Zheng, "Low-Dimensional Hybrid Perovskites for Field-Effect Transistors With Improved Stability: Progress and Challenges," *Advanced Electronic Materials* 6 (2020): 2000137, https://doi.org/10.1002/aelm.202000137.

11. H. Zhu, A. Liu, K. I. Shim, et al., "High-Performance Hysteresis-Free Perovskite Transistors Through Anion Engineering," *Nature Communications* 13 (2022): 1741, https://doi.org/10.1038/s41467-022-29434-x.

12. S. P. Senanayak, M. Abdi-Jalebi, V. S. Kamboj, et al., "A General Approach For Hysteresis-Free, Operationally Stable Metal Halide Perovskite Field-Effect Transistors," *Science Advances* 6 (2020): aaz4948, https://doi.org/10.1126/sciadv.aaz4948.

13. H. Zhu, W. Yang, Y. Reo, et al., "Tin Perovskite Transistors and Complementary Circuits Based on A-site Cation Engineering," *Nature Electronics* 6 (2023): 650–657, https://doi.org/10.1038/s41928-023-01019-6.

14. S. Maeng, S. J. Park, J. Lee, et al., "Direct Photocatalytic Patterning of Colloidal Emissive Nanomaterials," *Science Advances* 9 (2023): adi6950, https://doi.org/10.1126/sciadv.adi6950.

15. X. Niu, N. Li, Q. Chen, and H. Zhou, "Insights Into Large-Scale Fabrication Methods in Perovskite Photovoltaics," *Advanced Energy and Sustainability Research* 2 (2021), https://doi.org/10.1002/aesr.202000046.

16. Y. Kim, J. Woo, Y.-K. Jung, et al., "Reversible Oxidative p-Doping in 2D Tin Halide Perovskite Field-Effect Transistors," *ACS Energy Letters* 9 (2024): 1725–1734, https://doi.org/10.1021/acsenergylett.4c00497.

17. T. Kong, Y. Kim, J. Cho, et al., "Thermal Annealing-Induced Phase Conversion in N-type Triple-Cation Lead-Based Perovskite Field Effect Transistors," *ACS Applied Materials & Interfaces* 17 (2025): 8501–8512, https://doi.org/10.1021/acsami.4c17017.

18. H. Choi, S. Pecorario, Y. Zhang, H. Sirringhaus, and K. Kang, "Elucidating Contact-Limited Temperature Dependence of Charge Transport in 2D Tin Halide Perovskite Field-Effect Transistors," *Journal of Physics: Materials* 8 (2025), 2, https://doi.org/10.1088/2515-7639/adc33f.

19. P. Mathew, J. Cho, and P. V. Kamat, "Ramifications of Ion Migration in 2D LeadHalide Perovskites," *ACS Energy Letters* 9, no. 3 (2024), https://doi.org/10.1021/acsenergylett.4c00093.

20. Z. Wu and K. Leng, "Harnessing Ion Migration in 2D Perovskites for Fabricating Diode Heterostructure," *Matter* 7, no. 8 (2024): 2649–2651, https://doi.org/10.1016/j.matt.2024.04.046.

21. J. Schlipf, Y. Hu, S. Pratap, et al., "Shedding Light on the Moisture Stability of 3D/2D Hybrid Perovskite Heterojunction Thin Films," *ACS Applied Energy Materials* 2 (2019): 1011–1018, https://doi.org/10.1021/acsaem.9b00005.

22. E. S. Vasileiadou, B. Wang, I. Spanopoulos, I. Hadar, A. Navrotsky, and M. G. Kanatzidis, "Insight on the Stability of Thick Layers in 2D Ruddlesden–Popper and Dion–Jacobson Lead Iodide Perovskites," *Journal of the American Chemical Society* 143 (2021): 2523–2536, https://doi.org/10.1021/jacs.0c11328.

23. D. B. Mitzi, C. A. Feild, W. T. A. Harrison, and A. M. Guloy, "Conducting Tin Halides With a Layered Organic-based Perovskite Structure," *Nature* 369 (1994): 467–469, https://doi.org/10.1038/369467a0.

24. C. R. Kagan, D. B. Mitzi, and C. D. Dimitrakopoulos, "Organic-Inorganic Hybrid Materials as Semiconducting Channels in Thin-Film Field-Effect Transistors," *Science* 286 (1999): 945–947, https://doi.org/10.1126/science.286.5441.945.

25. H. Kim, C. B. Lee, B. H. Jeong, et al., "Alkylammonium Passivation For 2D Tin Halide Perovskite Field-Effect Transistors," *Journal of Materials Chemistry C* 13, no. 13 (2025): 6806–6815, https://doi.org/10.1039/d4tc05307a.

26. Y. Reo, H. Zhu, J.-Y. Go, et al., "Effect of Monovalent Metal Iodide Additives on the Optoelectric Properties of Two-Dimensional Sn-Based Perovskite Films," *Chemistry of Materials* 33 (2021): 2498–2505, https://doi.org/10.1021/acs.chemmater.0c04786.

27. H. Zhu, A. Liu, K. I. Shim, J. Hong, J. W. Han, and Y. Noh, "High-Performance and Reliable Lead-Free Layered-Perovskite Transistors," *Advanced Materials* 32 (2020): 2002717, https://doi.org/10.1002/adma.202002717.

28. L. Li, X. Liu, J. Guo, et al., "Low-Operating-Voltage Two-Dimensional Tin Perovskite Field-Effect Transistors With Multilayer Gate Dielectrics Based on a Fluorinated Copolymer," *The Journal of Physical Chemistry Letters* 14 (2023): 2223–2233, https://doi.org/10.1021/acs.jpclett.3c00072.

29. B. H. Jeong, J. A. Prayogo, J. Lee, et al., "Molecular Interlayer for High-Performance and Stable 2D Tin Halide Perovskite Transistor," *Advanced Science* 12, no. 26 (2025): 2409088, https://doi.org/10.1002/advs.202409088.

30. Z. Le, A. Liu, and H. Zhu, "Performance Enhancement of 2D Tin-halide Perovskite Transistors via Molecule-assisted Grain Boundary Passivation and Hole Doping," *Journal of Physics D: Applied Physics* 57 (2024): 275105, https://doi.org/10.1088/1361-6463/ad3b0a.

31. J.-Y. Go, H. Zhu, Y. Reo, H. Kim, A. Liu, and Y.-Y. Noh, "Sodium Incorporation for Enhanced Performance of Two-Dimensional Sn-Based Perovskite Transistors," *ACS Applied Materials & Interfaces* 14 (2022): 9363–9367, https://doi.org/10.1021/acsami.1c19368.

32. W.-J. Yin, T. Shi, and Y. Yan, "Unusual Defect Physics in CH3NH3PbI3 Perovskite Solar Cell Absorber," *Applied Physics Letters* 104 (2014): 063903, https://doi.org/10.1063/1.4864778.

33. J.-T. Lin, C.-C. Liao, C.-S. Hsu, et al., "Harnessing Dielectric Confinement on Tin Perovskites to Achieve Emission Quantum Yield up to 21%," *Journal of the American Chemical Society* 141 (2019): 10324–10330, https://doi.org/10.1021/jacs.9b03148.

34. C. Katan, N. Mercier, and J. Even, "Quantum and Dielectric Confinement Effects in Lower-Dimensional Hybrid Perovskite Semiconductors," *Chemical Reviews* 119 (2019): 3140–3192, https://doi.org/10.1021/acs.chemrev.8b00417.

35. L. Lanzetta, T. Webb, N. Zibouche, et al., "Degradation Mechanism of Hybrid Tin-based Perovskite Solar Cells and the Critical Role of Tin (IV) Iodide," *Nature Communications* 12 (2021): 2853, https://doi.org/10.1038/s41467-021-22864-z.

36. E. H. Kim, J. H. Lee, S. H. Kim, J. H. Gu, and D. Lee, "A-Site Effect on the Oxidation Process of Sn-Halide Perovskite: First-Principles Calculations," *The Journal of Physical Chemistry Letters* 12 (2021): 9691–9696, https://doi.org/10.1021/acs.jpclett.1c03033.

37. D. Meggiolaro, E. Mosconi, and F. D. Angelis, "Formation of Surface Defects Dominates Ion Migration in Lead-Halide Perovskites," *ACS Energy Letters* 4 (2019): 779–785, https://doi.org/10.1021/acsenergylett.9b00247.

38. G. Park, W. Yang, A. Liu, H. Zhu, F. D. Angelis, and Y.-Y. Noh, "High-performance Tin Perovskite Transistors Through Formate Pseudohalide Engineering," *Materials Science and Engineering: R: Reports* 159 (2024): 100806, https://doi.org/10.1016/j.mser.2024.100806.

39. F. Zhang, Q. Zhang, X. Liu, et al., "Property Modulation of Two-Dimensional Lead-Free Perovskite Thin Films by Aromatic Polymer Additives for Performance Enhancement of Field-Effect Transistors," *ACS Applied Materials & Interfaces* 13 (2021): 24272–24284, https://doi.org/10.1021/acsami.1c03041.

40. H. Zhu, A. Liu, T. Zou, H. Jung, S. Heo, and Y.-Y. Noh, "A Lewis Base and Boundary Passivation Bifunctional Additive for High Performance Lead-free Layered-perovskite Transistors and Phototransistors," *Materials Today Energy* 21 (2021): 100722, https://doi.org/10.1016/j.mtener.2021.100722.

41. J.-H. Cho, J.-Y. Go, T. T. Bui, et al., "Anion-Vacancy-Defect Passivation of a 2D-Layered Tin-Based Perovskite Thin-Film Transistor With Sulfur Doping," *Advanced Electronic Materials* 9 (2023): 2201014, https://doi.org/10.1002/aelm.202201014.

42. D. Ma, K. Lin, Y. Dong, et al., "Distribution Control Enables Efficient Reduced-dimensional Perovskite LEDs," *Nature* 599 (2021): 594–598, https://doi.org/10.1038/s41586-021-03997-z.

43. Y. Zhao, M. Li, X. Qin, P. Yang, W.-H. Zhang, and Z. Wei, "Efficient Perovskite Light-Emitting Diodes by Buried Interface Modification With Triphenylphosphine Oxide," *ACS Applied Materials & Interfaces* 15 (2023): 3644–3650, https://doi.org/10.1021/acsami.2c19123.

44. L. Na Quan, D. Ma, Y. Zhao, et al., "Edge Stabilization In Reduced-Dimensional Perovskites," *Nature Communications* 11 (2020): 170, https://doi.org/10.1038/s41467-019-13944-2.

45. T. Matsushima, M. R. Leyden, T. Fujihara, C. Qin, A. S. D. Sandanayaka, and C. Adachi, "Large Metal Halide Perovskite Crystals for Field-effect Transistor Applications," *Applied Physics Letters* 115 (2019): 120601, https://doi.org/10.1063/1.5116411.

46. T. Matsushima, S. Hwang, A. S. D. Sandanayaka, et al., "Solution-Processed Organic–Inorganic Perovskite Field-Effect Transistors With High Hole Mobilities," *Advanced Materials* 28 (2016): 10275–10281, https://doi.org/10.1002/adma.201603126.

47. J. C. Hamill, J. Schwartz, and Y.-L. Loo, "Influence of Solvent Coordination on Hybrid Organic–Inorganic Perovskite Formation," *ACS Energy Letters* 3 (2018): 92–97, https://doi.org/10.1021/acsenergylett.7b01057.

48. K. Hisatsune, S. Uchida, T. N. Murakami, and A. Kogo, "Effect of Br Ions in Octylammonium 2D Perovskites for Performance Improvement of CuSCN-Based Perovskite Solar Cells," *ACS Applied Energy Materials* 7 (2024): 5315–5320, https://doi.org/10.1021/acsaem.4c00692.

49. F. Yuan, X. Zheng, A. Johnston, et al., "Color-pure Red Light-emitting Diodes Based on Two-dimensional Lead-free Perovskites," *Science Advances* 6, no. 42 (2020): eabb0253, https://doi.org/10.1126/sciadv.abb0253.

50. Y. Ju, X. Wu, S. Huang, G. Dai, T. Song, and H. Zhong, "The Evolution of Photoluminescence Properties of PEA2SnI4 Upon Oxygen Exposure: Insight Into Concentration Effects," *Advanced Functional Materials* 32 (2022): 2108296, https://doi.org/10.1002/adfm.202108296.

51. Z.-Y. Zhang, H.-Y. Wang, Y.-X. Zhang, et al., "The Role of Trap-assisted Recombination in Luminescent Properties of Organometal Halide CH3NH3PbBr3 Perovskite Films and Quantum Dots," *Scientific Reports* 6 (2016): 27286, https://doi.org/10.1038/srep27286.

52. T. Liu, X. Zhao, J. Li, et al., "Enhanced Control of Self-doping in Halide Perovskites for Improved Thermoelectric Performance," *Nature Communications* 10 (2019): 5750, https://doi.org/10.1038/s41467-019-13773-3.

53. E. H. Kim, J. H. Lee, S. H. Kim, J. H. Gu, and D. Lee, "A-Site Effect on the Oxidation Process of Sn-Halide Perovskite: First-Principles Calculations," *The Journal of Physical Chemistry Letters* 12 (2021): 9691–9696, https://doi.org/10.1021/acs.jpclett.1c03033.

54. S. Kim, S. H. Kim, H. U. Hwang, et al., "Revisiting the Role of Oxidation in Stable and High-performance Lead-free Perovskite-IGZO Junction Field-effect Transistors," *Nature Communications* 16 (2025): 7427, https://doi.org/10.1038/s41467-025-62770-2.

55. R. Su, Z. Xu, J. Wu, et al., "Dielectric Screening in Perovskite Photovoltaics," *Nature Communications* 12 (2021): 2479, https://doi.org/10.1038/s41467-021-22783-z.

56. R. Szostak, S. Sanchez, P. E. Marchezi, et al., "Revealing the Perovskite Film Formation Using the Gas Quenching Method by in Situ GIWAXS:

Morphology, Properties, and Device Performance," *Advanced Functional Materials* 31 (2021): 2007473, https://doi.org/10.1002/adfm.202007473.

57. Y. Liu, P.-A. Chen, X. Qiu, et al., "Doping of Sn-based Two-dimensional Perovskite Semiconductor for High-performance Field-effect Transistors and Thermoelectric Devices," *iScience* 25, no. 4 (2022): 104109, https://doi.org/10.1016/j.isci.2022.104109.

58. S. Wang, Z. Ling, P. W. M. Blom, T. Marszalek, and W. Pisula, "Engineering Strategies for 2D Layered Tin Halide Perovskite Field-Effect Transistors," *Advanced Functional Materials* 35, no. 48 (2025): 2501217 , https://doi.org/10.1002/adfm.202501217.

59. W. Kohn and L. J. Sham, "Self-Consistent Equations Including Exchange and Correlation Effects," *Physical Review* 140 (1965): A1133–A1138, https://doi.org/10.1103/physrev.140.a1133.

60. G. Kresse and J. Furthmüller, "Efficiency of Ab-initio Total Energy Calculations for Metals and Semiconductors Using a Plane-wave Basis Set," *Computational Materials Science* 6 (1996): 15–50, https://doi.org/10.1016/0927-0256(96)00008-0.

61. G. Kresse and J. Furthmüller, "Efficient Iterative Schemes for Ab Initio Total-energy Calculations Using a Plane-wave Basis Set," *Physical Review B* 54 (1996): 11169–11186, https://doi.org/10.1103/physrevb.54.11169.

62. G. Kresse and D. Joubert, "From Ultrasoft Pseudopotentials To The Projector Augmented-Wave Method," *Physical Review B* 59 (1998): 1758–1775, https://doi.org/10.1103/physrevb.59.1758.

63. P. E. Blöchl, "Projector Augmented-Wave Method," *Physical Review B* 50 (1994): 17953–17979, https://doi.org/10.1103/physrevb.50.17953.

64. J. P. Perdew, K. Burke, and M. Ernzerhof, "Generalized Gradient Approximation Made Simple," *Physical Review Letters* 77 (1996): 3865–3868, https://doi.org/10.1103/physrevlett.77.3865.

65. S. Grimme, J. Antony, S. Ehrlich, and H. Krieg, "A Consistent and Accurate Ab Initio Parametrization of Density Functional Dispersion Correction (DFT-D) for the 94 Elements H-Pu," *The Journal of Chemical Physics* 132 (2010): 154104, https://doi.org/10.1063/1.3382344.

Supporting Information

Additional supporting information can be found online in the Supporting Information section.

Supporting File: adfm74094-sup-0001-SuppMat.pdf.